nature portfolio

https://doi.org/10.1038/s41586-021-03257-0

Supplementary information

Protecting a bosonic qubit with autonomous quantum error correction

In the format provided by the authors and unedited

Supplementary Information for
Protecting a Bosonic Qubit with Autonomous Quantum Error Correction

Jeffrey M. Gertler,[1] Brian Baker,[2] Juliang Li,[1] Shruti Shirol,[1] Jens Koch,[2] and Chen Wang*[1]
[1)] *Department of Physics, University of Massachusetts-Amherst, Amherst, MA, 01003, USA*
[2)] *Department of Physics and Astronomy, Northwestern University, Evanston, IL, 60201, USA*

(Dated: 4 November 2020)

1. BOSONIC CODE FOR APPROXIMATE AQEC

1.1. Applying PReSPA to Schrödinger-cat code ($|\alpha| \gg 1$)

Odd-parity cat states of the form $|C_\alpha^-\rangle = (|\alpha\rangle - |-\alpha\rangle)/N$, $|C_{i\alpha}^-\rangle = (|i\alpha\rangle - |-i\alpha\rangle)/N$ with large photon number, $|\alpha|^2 \gg 1$, can be used as cat-codes[1,2] that allow for perfect retrieval of information with an appropriate unitary. As shown in the following, single-photon loss followed by ideal PReSPA extended to infinite photon numbers

$$\hat{\Pi}'_{eo} = \sum_{n=0}^{\infty} |2n+1\rangle \langle 2n| \tag{S1}$$

preserves the capability to recover the initially stored quantum information.

Consider a general initial state $|\psi(0)\rangle = x\,|C_\alpha^-\rangle + y\,|C_{i\alpha}^-\rangle$ in the cat encoding. Within a given time period t, this state undergoes stochastic evolution governed by photon-loss events and continuous AQEC driving, resulting in a piece-wise deterministic process for $|\psi(t)\rangle$. Jump events are caused by photon loss, instantaneously followed by a PReSPA operation. In our analysis, we neglect the short time span $t_e \ll T_{1A}$ involved in the PReSPA operation itself. Under these conditions, the compound effect of photon loss and PReSPA is described by the jump operator $\hat{\Pi}'_{eo}\hat{a} = \sum_{n=0}^{\infty} \sqrt{2n+1}\,|2n+1\rangle\langle 2n+1|$. The deterministic time-evolution between jumps, as viewed from the rotating frame, is governed by the non-unitary operator

$$\hat{V}(t) = \exp\Big(-\frac{t}{2T_{1A}}\hat{a}^\dagger\hat{a}\Big). \tag{S2}$$

Note that $\hat{V}(t)$ decreases the cat size, $\alpha \to \tilde{\alpha}(t) = \alpha e^{-t/2T_{1A}}$. By contrast, photon loss/PReSPA events cause an increase in the mean photon number. For j loss/recovery events during time t, the final state is given by

$$|\psi_j(t)\rangle = x\,|C_{\tilde{\alpha},j}^-\rangle + y\,|C_{i\tilde{\alpha},j}^-\rangle\,, \tag{S3}$$

where $|C_{\tilde{\alpha},j}^-\rangle = (\hat{\Pi}'_{eo}\hat{a})^j\,|C_{\tilde{\alpha}}^-\rangle/N$. Although the latter are not perfect cat states anymore, they maintain parity and near orthogonality. Upon averaging over trajectories with different jump numbers j , one finds for the density matrix of the joint transmon-cavity system:

$$\hat{\rho}(t) = |g\rangle\langle g| \otimes \sum_j p_j(t)\,|\psi_j(t)\rangle\langle\psi_j(t)| = |g\rangle\langle g| \otimes (x + ye^{i\pi a^\dagger a/2}) \sum_j p_j(t)\,|C_{\tilde{\alpha},j}^-\rangle\,\langle C_{\tilde{\alpha},j}^-|\,(x^* + y^* e^{-i\pi a^\dagger a/2}). \tag{S4}$$

Here, $p_j(t)$ is the probability for j loss/recovery events to occur during time t.

For recovery of the amplitudes x and y to succeed, $|C_{\tilde{\alpha},j}^-\rangle$ and $|C_{i\tilde{\alpha},k}^-\rangle$ should be orthogonal $\forall j,k$. Since $\langle C_{i\tilde{\alpha},j}^-|C_{\tilde{\alpha},k}^-\rangle \propto e^{-|\tilde{\alpha}|^2}\sin\big(|\tilde{\alpha}|^2\big)$, (near-)orthogonality is given for $|\alpha|^2 \gg 1$. Accordingly, the cavity Hilbert space splits into two orthogonal subspaces, with $|C_{\tilde{\alpha},j}^-\rangle \in \mathcal{H}_1$, $|C_{i\tilde{\alpha},j}^-\rangle \in \mathcal{H}_2$, and the prescriptions $|g\rangle \otimes |C_{\tilde{\alpha},j}^-\rangle \to |g\rangle \otimes |C_{\tilde{\alpha},j}^-\rangle$, $|g\rangle \otimes |C_{i\tilde{\alpha},j}^-\rangle \to |e\rangle \otimes e^{-i\pi a^\dagger a/2}\,|C_{i\tilde{\alpha},j}^-\rangle$, are compatible with a unitary decoding transformation. Once applied to the state (S4), this yields

$$\hat{\rho}_d = \hat{U}_d\hat{\rho}\hat{U}_d^\dagger = (x\,|g\rangle + y\,|e\rangle)(x^*\,\langle g| + y^*\,\langle e|) \otimes \sum_j p_j\,|C_{\tilde{\alpha},j}^-\rangle\,\langle C_{\tilde{\alpha},j}^-|\,, \tag{S5}$$

leaving the transmon qubit in the desired pure state $x\,|g\rangle + y\,|e\rangle$.

1.2. Evolution of truncated 4-component cat (T4C) states under photon loss and PReSPA

Our T4C encoding is an instance of the single-cavity binomial code[3]. It can also be understood as a cat code with $|\alpha|^2 \approx 3.5$ truncated at a photon number cutoff at 7. Here, we encode the quantum information in the superposition $|\psi(0)\rangle = x\,|0_L\rangle + y\,|1_L\rangle$, where the logical code words are

$$|0_L\rangle = C_1\,|1\rangle + C_5\,|5\rangle\,, \qquad |1_L\rangle = C_3\,|3\rangle + C_7\,|7\rangle\,. \tag{S6}$$

The effective jump operator for loss/recovery events is a truncation of the original $\hat{\Pi}'_{eo}\hat{a}$, namely $\hat{\Pi}_{eo}\hat{a} = |1\rangle\langle 1| + \sqrt{3}\,|3\rangle\langle 3| + \sqrt{5}\,|5\rangle\langle 5| + \sqrt{7}\,|7\rangle\langle 7|$. The resulting quantum trajectory given j events is

$$|\psi_j(t)\rangle = \frac{1}{N_j(t)}\Big[x\sum_{n=1,5} + y\sum_{n=3,7}\Big] C_n n^{j/2} e^{-nt/2T_{1A}}\,|n\rangle\,, \tag{S7}$$

where $N_j(t)$ is the time-dependent normalization factor. Note that the trajectory (S7) exhibits no dependence on the specific jump times, because the jump operator $\hat{\Pi}_{eo}\hat{a}$ commutes with the deterministic evolution operator (S2). To compare Eq. (S7) with (S3), we rewrite the trajectory state as a superposition of two states from the orthogonal subspaces $\mathcal{H}_{15} = \mathrm{span}\{|1\rangle, |5\rangle\}$ and $\mathcal{H}_{37} = \mathrm{span}\{|3\rangle, |7\rangle\}$, namely

$$|\psi_j(t)\rangle = x\,n_j^{15}(t)\,|\psi_j^{15}(t)\rangle + y\,n_j^{37}(t)\,|\psi_j^{37}(t)\rangle\,. \tag{S8}$$

Here, $\big|\psi_j^{kl}(t)\big\rangle = \sum_{n=k,l} C_n n^{j/2} e^{-nt/2T_{1A}}\,|n\rangle\,/[n_j^{kl} N_j(t)]$ are orthonormal, and $n_j^{kl}(t) = \|\sum_{n=k,l} C_n n^{j/2} e^{-nt/2T_{1A}}\,|n\rangle\,\|/N_j(t)$.

As a side note, although the mean photon numbers $\bar{n}$ varies from trajectory to trajectory, the ensemble-averaged photon number, $\langle\bar{n}\rangle$, of a cavity state is conserved under the combined effect of $\hat{\Pi}_{eo}\hat{a}$. This is because the operator $\hat{\Pi}_{eo}\hat{a}$ is a (diagonal) dephasing-type of jump operator that does not extract or supply energy to the system. One can also conveniently prove this by checking the diagonal vector of the Lindblad master equation, and see for any density matrix ρ: $\mathrm{diag}[\dot{\rho}] \propto \mathrm{diag}[\mathcal{L}(\hat{\Pi}_{eo}\hat{a}, \rho)] = 0$.

1.3. T4C decoding unitary for approximate quantum information retrieval

Given the distortion due the $n_j^{kl}(t)$ coefficients, as well as the rotations within the $\mathcal{H}_{15}$ and $\mathcal{H}_{37}$ subspaces, to what degree does it remain possible to decode the original quantum information? The answer and mitigation strategy depends on the elapsed time t. Here, we focus on short times $t/T_{1A} \ll 1$, for which only small jump numbers j are relevant. [For $t/T_{1A} \ll 1$, $p_j(t)$ is peaked at $j = 0$ and falls off rapidly as j increases. These jump probabilities are given by $p_j(t) = (t/T_{1A})^j N_j^2(t)/j!$]

We divide our discussion into two parts, addressing the distortion coefficients and spurious rotations separately. Starting with the former, we note that the distortion via $n_j^{kl}(t)$ is not observed in Eq. (S3) for the cat code. For the T4C scheme the distortion originates from the truncation to small photon numbers. We may mitigate this issue by choosing the code-word amplitudes C_n is such a way as to minimize distortion, i.e., make the relevant $n_j^{kl}(t)$ as close to unity as possible. Expanding numerator and denominator of $(n_0^{kl})^2$ $\big[(n_0^{15})^2$ or $(n_0^{37})^2\big]$ for $t/T_{1A} \ll 1$ yields the intermediate expression

$$[n_0^{kl}(t)]^2 = \frac{1 - t/T_{1A}\langle n\rangle_{kl} + \frac{(t/T_{1A})^2}{2}\langle n^2\rangle_{kl} + \mathcal{O}((t/T_{1A})^3)}{x^2\big[1 - t/T_{1A}\langle n\rangle_{15} + \frac{(t/T_{1A})^2}{2}\langle n^2\rangle_{15} + \mathcal{O}((t/T_{1A})^3)\big] + y^2\big[1 - t/T_{1A}\langle n\rangle_{37} + \frac{(t/T_{1A})^2}{2}\langle n^2\rangle_{37} + \mathcal{O}((t/T_{1A})^3)\big]}\,, \tag{S9}$$

where $\langle n^m\rangle_{kl}$ is the m-th moment of the photon number probability distribution, with probabilities $|C_k|^2$ and $|C_l|^2 = 1 - |C_k|^2$. This expression reveals that $n_0^{kl} = 1$ up to second order in t/T_{1A} if the mean and second moments obey $\langle n\rangle_{15} = \langle n\rangle_{37}$ and $\langle n^2\rangle_{15} = \langle n^2\rangle_{37}$. These two conditions, along with the normalization requirement, fully determine the optimal choices for the code-word amplitudes: $C_1 = C_7 = 1/2$ and $C_3 = C_5 = \sqrt{3}/2$. (The choice $C_1 = \sqrt{0.35}$, $C_5 = \sqrt{0.65}$, $C_3 = \sqrt{0.9}$, and $C_7 = \sqrt{0.1}$ used in the experiments yields mean photon numbers of 3.6 and 3.4, and second moments of 16.6 and 13, constituting a reasonable, though not optimum, choice.) Expansion to higher orders in t/T_{1A} as well as consideration of jump numbers $j > 0$ lead to additional conditions $\langle n^m\rangle_{15} = \langle n^m\rangle_{37}$ with $m > 2$, which cannot be satisfied anymore.

Second, we consider the spurious rotations within each code-word subspace, while focusing on the construction of a suitable decoding unitary. For $t/T_{1A} \ll 1$ and small jump numbers, this unitary $\hat{U}_d$ should approximately map the state (S8) to a product state, in which the transmon occupies the state $x\,|g\rangle + y\,|e\rangle$, i.e.

$$|\Psi_j(t)\rangle = |g\rangle \otimes \big(xn_j^{15}(t)\,\big|\psi_j^{15}(t)\big\rangle + yn_j^{37}(t)\,\big|\psi_j^{37}(t)\big\rangle\big) \xrightarrow{\hat{U}_d} |\Psi_j(t)\rangle_d \approx \big(x\,|g\rangle + y\,|e\rangle\big) \otimes |\phi_j\rangle\,, \tag{S10}$$

where the cavity states $|\phi_j(t)\rangle$ must be consistent with the unitarity of U_d, but can otherwise be chosen at will. To approximate this transformation, we select orthonormal bases of the two code-word subspaces, $\mathcal{H}_{15} = \mathrm{span}\{|u_0\rangle, |u_1\rangle\}$ and $\mathcal{H}_{37} = \mathrm{span}\{|v_0\rangle, |v_1\rangle\}$, and choose U_d to map

$$|g\rangle \otimes |u_0\rangle \to |g0\rangle\,, \quad |g\rangle \otimes |u_1\rangle \to |g1\rangle\,, \quad |g\rangle \otimes |v_0\rangle \to |e0\rangle\,, \quad |g\rangle \otimes |v_1\rangle \to |e1\rangle\,. \tag{S11}$$

We only specify $\hat{U}_d$ for these 4 basis states relevant to the T4C code, leaving the rest undetermined. Decomposed in this basis, the evolved T4C state reads

$$|\Psi_j(t)\rangle = |g\rangle \otimes x\,n_j^{15}(t)\big(\cos\theta_j\,|u_0\rangle + \sin\theta_j\,|u_1\rangle\big) + y\,n_j^{37}(t)\big(\cos\varphi_j\,|v_0\rangle + \sin\varphi_j\,|v_1\rangle\big), \tag{S12}$$

where the angles θ_j and φ_j parametrize the states $|\psi_j^{kl}(t)\rangle$ (see main text, Extended Data Fig. 1a). The state resulting after application of the decoding unitary is

$$|\Psi_j(t)\rangle_d = \hat{U}_d\,|\Psi_j(t)\rangle = x\,n_j^{15}(t)\,|g\rangle \otimes \big(\cos\theta_j\,|0\rangle + \sin\theta_j\,|1\rangle\big) + y\,n_j^{37}(t)\,|e\rangle \otimes \big(\cos\varphi_j\,|0\rangle + \sin\varphi_j\,|1\rangle\big). \tag{S13}$$

The decoding fidelity can in principle be optimized by a suitable choice of the cavity states $|u_k\rangle$, $|v_k\rangle$. Here, we omit optimization and simply select the original code-words as basis states, $|u_0\rangle = |0_L\rangle$ and $|v_0\rangle = |1_L\rangle$. This is appropriate for $t/T_{1A} \ll 1$ where small jump numbers dominate. From series expansion of $\cos^2\theta_0 = |\left\langle 0_L \middle| \psi_0^{15} \right\rangle|^2$ and $\cos^2\varphi_0 = |\left\langle 1_L \middle| \psi_0^{37} \right\rangle|^2$, one finds $\theta_0 = \varphi_0 + \mathcal{O}((t/T_{1A})^2)$ if the optimum code-word amplitudes C_n are employed. Imperfections in decoding do arise in the small-time limit for larger jump numbers. Following the decoding operation, the reduced density matrix of the transmon takes on the form

$$\hat{\rho}_q = \mathrm{Tr}_{\text{cavity}}\left(\hat{U}_d \sum_j p_j\,|\Psi_j\rangle\langle\Psi_j|\,\hat{U}_d^\dagger\right) = \sum_j p_j \begin{pmatrix} |x|^2 (n_j^{15})^2 & x^* y n_j^{15} n_j^{37}\cos(\theta_j - \varphi_j) \\ x y^* n_j^{15} n_j^{37}\cos(\theta_j - \varphi_j) & |y|^2 (n_j^{37})^2 \end{pmatrix}, \tag{S14}$$

where time dependence is implied but not shown explicitly to simplify notation.

$\hat{\rho}_q$ is a good short-time approximation to the intended state $|\psi_q\rangle\langle\psi_q|$. The deviation between the two is quantified by the process fidelity that is obtained from averaging the state-transfer fidelity $\mathcal{F}_{xy}(t) = |\langle\psi_q|\hat{\rho}_q(t)|\psi_q\rangle|^2$ over the six cardinal points on the Bloch sphere and then rescaled to the range from 1/4 to 1,

$$\mathcal{F}_{\text{process}}(t) = \frac{3}{2}\langle\mathcal{F}_{xy}(t)\rangle - \frac{1}{2}, \tag{S15}$$

where $\langle\mathcal{F}_{xy}(t)\rangle$ is the Bloch sphere average. Future work may include optimization of this fidelity with respect to the choice of decoding basis states.

2. OPTIMAL CONTROL FOR UNITARY OPERATIONS AND STATE TRANSFER

Pulses for state preparation and decoding are constructed using quantum optimal control (QOC)[4–7], designed to steer the time evolution of a quantum system in order to maximize the fidelity of the desired state transfer or unitary operation. More specifically, QOC iteratively adjusts the set of control pulses $\{u_1(t), \ldots, u_M(t)\}$ in a way that minimizes the deviations between the realized unitary $\hat{U}$ and the target unitary $\hat{U}_T$ (or between realized state $|\psi\rangle$ and target state $|\psi_T\rangle$). The concrete quantity to be minimized is the cost functional $C[\{u_k(t)\}]$, which incorporates the process or state infidelity, as well as additional cost contributions crucial for achieving realistic pulse shapes. We employ an automatic-differentiation extension[8] of GRAPE (Gradient Ascent Pulse Engineering)[9], which performs minimization via gradient descent. In the following, we provide additional details on the implementation.

For numerics, the control fields are reduced to a finite number of optimization parameters by discretization of the time axis: the pulse duration t_d is split into a number $N \gg 1$ of small time intervals (here: $\delta t = 1\,\text{ns}$). The corresponding discrete time instances are denoted $t_n = n\delta t$, along with the control amplitudes evaluated at these times, $u_{kn} = u_k(t_n)$. The latter can now be grouped into a vector $\mathbf{u} = (u_{kn}) \in \mathbb{R}^{MN}$ containing all optimization parameters. The primary quantity for optimization is either the process fidelity (target unitary, such as for decoding) or the state-transfer fidelity (target state, such as for preparation of specific cavity state). These are defined as

$$\mathcal{F}_{\text{decoding}}(\mathbf{u}) = \frac{1}{D^2}|\mathrm{Tr}(\hat{U}_T^\dagger \hat{U}(\mathbf{u}))|^2, \tag{S16}$$

$$\mathcal{F}_{\text{prep}}(\mathbf{u}) = |\langle\psi_T|\psi(\mathbf{u})\rangle|^2, \tag{S17}$$

where $D = 7$, the dimension of the subspace considered for the decoding operation. The realized unitary or state is computed by decomposing the evolution operator $\hat{U}_f$ governing the full duration t_d into short-time propagators $\hat{U}_n = \exp(-i\hat{H}_n\delta t)$ describing the unitary evolution of the system from time t_n to $t_n + \delta t$,

$$\hat{U}_f = \hat{U}_N \hat{U}_{N-1} \cdots \hat{U}_1 \hat{U}_0. \tag{S18}$$

Each short-time propagator only involves the Hamiltonian evaluated at time t_n,

$$\hat{H}_n = \hat{H}(t = t_n) = \hat{\mathcal{H}}_0 + \sum_{k=1}^{M} u_{kn}\hat{\mathcal{H}}_k \tag{S19}$$

with $\hat{\mathcal{H}}_0$ denoting the time-independent system Hamiltonian and $\{\hat{\mathcal{H}}_k\}$ the set of control operators. In our case, the latter correspond to the transmon and cavity operators $\{\hat{\sigma}_x, \hat{\sigma}_y, \hat{x}_A, \hat{p}_A\}$, and the static system Hamiltonian is given by

$$\hat{\mathcal{H}}_0 = -\frac{\chi_q}{2}\hat{a}^\dagger\hat{a}\hat{\sigma}_z - \frac{K}{2}\hat{a}^\dagger\hat{a}^\dagger\hat{a}\hat{a} - \frac{\chi_q'}{4}\hat{a}^\dagger\hat{a}^\dagger\hat{a}\hat{a}\hat{\sigma}_z \tag{S20}$$

in the appropriate rotating frame. The coefficients K, χ_q, χ_q' parametrize the self-Kerr, 4$^{\text{th}}$-order cross-Kerr, and 6$^{\text{th}}$-order cross-Kerr terms, respectively.

In addition to the primary contribution $C_1 = 1 - \mathcal{F}$ to the cost function, i.e. the process or transfer infidelity, it is beneficial to incorporate secondary cost contributions which favor pulse shapes compatible with experimental capabilities and constraints. One secondary cost contribution,

$$C_2 = \sum_{k,n} |u_{kn} - u_{kn-1}|^2, \tag{S21}$$

penalizes rapid temporal changes of the pulse envelopes, thus helping to limit overall pulse bandwidth. Another secondary cost contribution we employ is

$$C_3 = \sum_{k,n} |u_{kn}|^2, \tag{S22}$$

which limits the overall pulse power. Finally, we introduce a cost for occupation of certain higher states $|\psi_F\rangle$ ("forbidden" states). This can, for example, minimize leakage of the transmon into states outside the $\{|g\rangle, |e\rangle\}$ logical subspace, and generally help avoid any population close to the Hilbert space truncation level (truncation levels used were 3 and 24 for the transmon and cavity Hilbert space, respectively). The corresponding cost contribution is

$$C_4 = \sum_{n} |\langle\psi_F|\psi_n\rangle|^2, \tag{S23}$$

where $|\psi_n\rangle$ is the state at time t_n. The total cost function to be minimized is a weighted sum of the individual contributions,

$$C(\mathbf{u}) = C_1(\mathbf{u}) + \alpha_2 C_2(\mathbf{u}) + \alpha_3 C_3(\mathbf{u}) + \alpha_4 C_4(\mathbf{u}). \tag{S24}$$

In its basic form, gradient descent minimizes $C(\mathbf{u})$ by repeatedly updating $\mathbf{u}$ with a vector opposite to the cost function gradient,

$$\mathbf{u}_{p+1} = \mathbf{u}_p - \eta_p \frac{\partial C(\mathbf{u}_p)}{\partial \mathbf{u}_p}. \tag{S25}$$

Here, we use ADAM[10], a "momentum accelerated" gradient-descent method which updates $\mathbf{u}$ using a moving average of both the gradient direction and magnitude. To make convergence properties more stable, we apply the common strategy of a decaying learning rate $\eta_p = \eta_0 e^{-\beta p}$. Gradients $\partial C(\mathbf{u}_p)/\partial \mathbf{u}_p$ are computed using a TensorFlow-supported automatic differentiation algorithm[11]. Rather than hard-coding analytical gradients, this algorithm decomposes $C(\mathbf{u}_p)$ into a computational graph of elementary functions, whose known derivatives are extracted via the chain rule through a back-propagation process.

For bootstrapping, we used Gaussian white noise as initial pulses $\mathbf{u}_0$ in order to avoid bias towards any particular pulse shape. Computations were carried out on a CPU with a step count of $N = t_d/\delta t$. For state preparation, $t_d = 1\,\mu$s and for decoding, $t_d = 2\,\mu$s. The total number of iterations to achieve sufficient fidelity convergence typically ranged from 1,000-2,000, thus requiring only moderate computation times of a few hours.

3. ERROR SOURCES OF THE CORRECTED LOGICAL QUBIT

The errors in the autonomously corrected logical qubit can be divided into two main categories: 1) errors unrelated to single photon loss that are not yet corrected by our AQEC scheme, and 2) errors caused by various failure modes of our AQEC scheme while it corrects single photon loss. A breakdown of the contributions from various error mechanisms is listed in Extended Data Table III. The total effect is consistent with the experimentally measured longitudinal ($366 \pm 10\,\mu$s) and transverse ($256 \pm 7\,\mu$s) relaxation times of the logical qubit within 5%.

3.1. Photon-loss unrelated errors

Cavity dephasing is not correctable with the PReSPA scheme. The dominant source of cavity dephasing is spontaneous excitation (the rate $\gamma_\uparrow$) of the ancilla transmon from its ground state to excited states, which we believe is caused by stray radiation from the microwave transmission line. In addition to its dephasing effect to the cavity (due to the dispersive Hamiltonian $-\chi_q \hat{a}^\dagger \hat{a} \frac{\sigma_z}{2}$), an ancilla $\gamma_\uparrow$ event may trigger an odd-to-even photon addition process under PReSPA due to the relative lack of photon-number selectivity in the second stage of the pumping process (Extended Data Fig. 6a). This process erroneously switches the cavity to the even-parity sub-space, which will immediately gain another photon under PReSPA. Effectively, each $\gamma_\uparrow$ jump has a substantial probability to induce the addition of two photons to the cavity state, moving the cavity state between the $\{|1\rangle, |5\rangle\}$ subspace and the $\{|3\rangle, |7\rangle\}$ subspace, which is a bit flip error for logical pole states. From competition of relevant rates in this multi-stage process, we estimate this probability to be about 50%. For logical equator states, $\gamma_\uparrow$ produces a transverse relaxation error by fully dephasing the cavity. In total, our AQEC scheme, as currently constructed, leaves the logical qubit modestly more susceptible to $\gamma_\uparrow$ of the ancilla compared with a bare cavity using Fock states $|0\rangle$ and $|1\rangle$ to store information.

Strong parametric pumping as used in our mixing tone increases spurious transmon excitation. We observe an increase in transmon $\gamma_\uparrow$ rate by about 30% under long-time pumping of the mixing comb, from 1.4 ms^{-1} in the idle state to 1.8 ms^{-1}, as extracted from a set of specifically designed experiments probing spurious cavity excitations (Extended Data Fig. 6b-e). We note that all mixing tones in PReSPA combined (computed as the sum of $|\xi_i|$) are still weaker than reported thresholds for causing spurious transmon excitations in prior experiments[12–14], so it is likely that the observed heating effect is extrinsic and reducible by better thermalization. In addition, we estimate that the pump-induced linear displacement to the transmon operator $\hat{q}$ should contribute negligibly to spurious transmon excitations. However, we cannot rule out contributions from non-perturbative dynamics of a driven Josephson circuit[15], especially considering a comb of multiple pump tones may cause additional complexities in the dynamics beyond what has been reported so far. This scenario corresponds to a fundamental limitation of using a transmon as a parametric mixer, and motivates the adoption of novel types of ancillas in future AQEC experiments. Nevertheless, a future iteration of better-optimized transmon-based PReSPA protocol with better coherence properties will employ weaker (rather than stronger) pumping than the current demonstration, hence alleviating this concern of pump-induced spurious excitations. (See Methods-AQEC Simulations.)

Separately, the transmon comb of PReSPA has an intrinsic effect of exciting the transmon off-resonantly when the cavity is in the odd-parity code space. With our parameters, this effect is weak compared with other $\gamma_\uparrow$ effects and difficult to experimentally characterize, but we determine it to be slightly lower than 0.2 ms^{-1} from numerical simulations. This excitation rate can be estimated as $\gamma_m(\lambda/\chi_q)^2$, where γ_m is the transmon decay rate through the four-wave mixing process. In the long run, this intrinsic effect requires trade-off in the QEC operation speed. It is important to note that its scaling is to the third power of the QEC operation speed if we scale λ, Ω, κ proportionally, as we confirmed in simulations.

3.2. Photon-loss correction efficiency

PReSPA is designed to correct for single photon loss, which occurs on a timescale of $T_{1A}/\bar{n} \approx 150$ μs in our T4C-encoded logical qubit and induces both longitudinal and transverse errors. An intuitive quantity to evaluate the efficacy of this correction process is the QEC success rate, S_l or S_t, as we defined in the main text. It represents the fraction of photon-loss errors whose impact to the logical qubit is successfully eliminated by the AQEC scheme. For the convenience of arguments, we imagine that each photon loss occurring to the T4C qubit, when uncorrected, induce a single depolarization error from anywhere on the Bloch sphere (equivalent to a longitudinal relaxation error for pole state and a transverse relaxation error for an equator state). This is in fact a decent approximation for the uncorrected T4C code.

In the absence of any error unrelated to photon loss, the corrected logical qubit lifetime is equal to the inversely averaged relaxation time of the 6 cardinal-point states of the Bloch sphere:

$$\tau_C = \frac{6}{4\Gamma_t + 2\Gamma_l} = \frac{T_{1A}}{\bar{n}} \frac{1}{1 - \frac{2}{3}S_t - \frac{1}{3}S_l} \tag{S26}$$

where we have used $\Gamma_i = \frac{\bar{n}}{T_{1A}}(1 - S_i)$ by our definition of S_i. On the other hand, the Fock $|0/1\rangle$ encoding has lifetime of $\tau_{01} = \frac{3}{2}T_{1A}$. Hence to reach break-even the overhead factor due to redundant encoding one has to overcome is $3\bar{n}/2$. From $\tau_C > \tau_{01}$, a necessary requirement for QEC break-even is:

$$\frac{1}{3}S_l + \frac{2}{3}S_t > 1 - \frac{2}{3}\bar{n}^{-1} \tag{S27}$$

We note that due to intrinsic off-resonant excitation of transmon in our current PReSPA scheme, error channels not attributed to photon loss cannot be fully eliminated. This effect, together with other types of uncorrectable errors, means that a greater success rate than indicated by Eq. (S27) is needed to achieve break-even. However, this minimum threshold still serves as a useful benchmark to consider the performance of a QEC process in correcting the errors it is designed to correct.

An ideal (infinitely-fast) implementation of PReSPA dissipation using a perfect ancilla can fully eliminate longitudinal errors and correct transverse errors at 97.5% success probability (see Methods-Approximate AQEC). Experimentally, there are multiple other failure modes associated with the photon-loss-correction process, as listed in Extended Data Table III, adding up to an estimated total of 11% and 24% failure rates for correcting pole and equator states in this work. (This corresponds to $S_l = 89\%$ and $S_t = 76\%$ as discussed in the main text.)

Relaxation of the ancilla and the loss of a second photon during the correction process account for a significant part of the failure rates. During each error-correction process, the probability of transmon T_1 decay can be computed as $\int P_e(t)dt/T_{1q} = 7\%$, where $P_e(t)$ is the transmon excitation probability (Fig. S1). The probability of a second photon decay can be estimated as $t_{eo}\bar{n}/T_{1A} = 5.6\%$, where t_{eo} is the halftime of the error-correction process. Since a second photon decay is a bit-flip error, its reduction to S_l is twice of its occurrence rate, or about 11%. These failure rates are dictated by the competition between the speed of the QEC operation and the hardware coherence, and can be expected to improve proportionally with better transmon and cavity lifetime.

In addition, there are several failure modes associated with the competing time scales in PReSPA. Firstly, the pumping process can be activated virtually by a neighboring mixing tone that is $2\chi_q$ detuned from the resonance condition, causing cavity dephasing. This occurs at an estimated 3% probability based on the relative rates of the virtual (unintended) *vs.* resonant (intended) four-wave-mixing transitions, and scales as $(\kappa/2\chi_q)^2$. In our experiment, κ can be reduced by at least $\sim$20% without compromising the speed of the AQEC operation, hence improving overall AQEC performance.

Secondly, due to the stochastic nature of the dissipative correction process, the cavity spends an uncertain period of time in the even-parity error space. This time uncertainty δt_{eo} is smaller than but scales linearly with the average correction time t_{eo}. It multiplies with the self-Kerr (K) of the cavity Hamiltonian to produce a phase uncertainty to the PReSPA operator, and hence a logical dephasing error to the QEC process.

Furthermore, in the presence of other higher-order nonlinear effects from χ_q' and χ_{Ar}, the two groups of intermediate states in the PReSPA dynamics ($|2n, e, 0\rangle$ and $|2n+1, g, 1\rangle$) are not equally spaced. One might expect them to cause which-path information leakage due to reservoir photon emissions at different frequencies. However, the actual effect is more subdued: In a dissipative Λ transition, the emission frequency is solely dictated by the energy difference of initial/final states and energy supplied by the drives, not the intermediate levels. (The energy differences due to Kerr is already accounted for, see the paragraph above). This is a technique to promote path-independence using slightly-virtual transitions[16]. In this scenario, because the quantum states do not transit through the intermediate states exactly on resonance, there is a subtle geometric phase uncertainty causing a relatively small dephasing effect. The scaling of this residual error has been analyzed in detail in Appendix C of Ref.[16], which applied to the present cases is $(\chi_q'/\gamma_m)^2$ and $(\chi_{Ar}/\kappa)^2$ respectively. Here $\gamma_m \approx 0.35\ \mu\mathrm{s}^{-1}$ is the rate of transmon decay via the reservoir due to the mixing comb.

Our AQEC process is insensitive to dephasing (T_ϕ) error of the ancilla. Owing to the mirrored dynamics of the four photon-addition paths in PReSPA, a phase jump of the transmon ancilla during the photon addition resets the process but does not cause cavity dephasing. The net effect is a small reduction of the correction rate of PReSPA, which can be compensated by choosing a larger λ. Similarly, low-frequency (*i.e.* $1/f$) noise of the ancilla does not affect PReSPA performance to the first order either. This insensitivity to ancilla dephasing has an interesting correspondence to the scenario in measurement-based bosonic QEC, where a T_ϕ error leads to a parity (error syndrome) measurement error but does not propagate forward to the cavity state[17]. This type of error in discrete parity measurements in principle can be mitigated by repetition and majority voting, which however, amplifies other types of errors (such as ancilla T_1) and are typically undesirable in experiments[17,18]. In comparison, our continuous AQEC protocol effectively repeats its error detection process automatically until it succeeds with minimal overhead.

4. ERROR RECOVERY TEST

In the process of tuning up PReSPA, we developed an experiment to evaluate the efficiency of PReSPA in performing a single QEC operation. To do this we prepare with an OCT pulse the "ideal error state":

$$|\psi_e\rangle = \frac{1}{\sqrt{2}}(C_1 |0\rangle + e^{i\phi_3} C_3 |2\rangle + e^{i\phi_5} C_5 |4\rangle + e^{i\phi_7} C_7 |6\rangle). \tag{S28}$$

This is a state that the ideal PReSPA operator (Eq. (2) of the main text) will correct back to the $|X\rangle_L$ state after 25 μs. The phases ϕ_3, ϕ_5 and ϕ_7 are chosen to compensate for the phase accumulation due to the cavity self-Kerr.

After applying 25 μs of PReSPA, we use the decoding unitary to map the logical state to the transmon, and measure the $\hat{\sigma}_x$ projection. To compensate for the loss in fidelity due to encoding and decoding we perform a separate experiment of encoding and immediately decoding a logical $|x\rangle_L$ state before taking a $\hat{\sigma}_x$ projection. By comparing the results of these two measurements we measure a normalized fidelity of the recovered state $F = 67 \pm 2\%$.

This measurement is analogous to characterization of the PReSPA process χ-matrix, which includes additional errors accumulated over the 25 μs process time in addition to the one-time parity restoration process. It is therefore in direct agreement with the 67% average preservation of phase coherence in Fig. 3. It is also consistent with the success probability $S_t = 76\%$ for a one-time PReSPA operation after accounting for the compounded 10% fidelity loss from all transverse error channels.

5. PRESPA OPTIMIZER FOR LOGICAL EQUATOR STATES

To achieve a better choice of PReSPA control parameters (the amplitudes and phases of microwave tones) we implement an empirical optimization routine. The ultimate goal of our optimization is to decrease the decay rate of the process fidelity to increase AQEC efficiency. For this we initialize a logical state, apply 144 μs of PReSPA, decode the state and perform transmon tomography. We can optimize this fidelity by slightly varying a PReSPA control parameter and performing this procedure. By iterating over each PReSPA control parameter, we can gradually optimize the AQEC scheme. Experimentally we find that the logical equator states ($|X\rangle_L$, $|-X\rangle_L$, $|Y\rangle_L$, $|-Y\rangle_L$) are more susceptible to small changes in PReSPA parameters than the pole states ($|Z\rangle_L$, $|-Z\rangle_L$). Because of this, we choose our optimization cost function to be a mean of the fidelities of these four states.

This optimization was implemented to choose control parameters used for PReSPA-2 in Extended Data Fig. 4. We achieved a slight gain in logical coherence time over PReSPA-1, whose control parameters were only chosen using the calibration experiments described in the methods section. While better for logical lifetimes, we observed that the PReSPA-2 rates (Ω_n and λ_n) were less well matched than those for PReSPA-1. Further work is needed to understand how a dissipative operator that deviates from Eq. (2) can achieve better AQEC performance.

6. ALL ABOUT READOUT

To readout the transmon state we perform a heterodyne measurement on the readout cavity state looking for a disspersive shift in its frequency dependant on transmon state. This signal is amplified by a Traveling Wave Parametric Amplifier[19] (TWPA) from MIT Lincoln Laboratory, a LNF-LNC4_8C cryogenic low-noise amplifier and a MITEQ room-temperature amplifier, but we do not have the signal-to-noise ratio optimized sufficiently to perform single-shot readout. Instead we measure the transmission signal with the transmon prepared in the nominal ground and excited states to measure the contrast by which we convert raw, averaged signals to excited state population measurements.

The nominal ground state of the transmon is its equilibrium prepared by waiting for a sufficiently long time ($>$10 T_{1q}) for the transmon to decay, and the nominal excited state is obtained by π-pulsing the qubit from its nominal ground state. Since our transmon has a 5% excited state population in equilibrium, this means that all reported quantum state fidelity should be understood as scaled up by 10% compared to the true pure target state. However, since all the main results reported in this manuscript focus on the relative change between two states, such as process fidelity or decay time, this factor affects measurements of both states proportionally and therefore does not affect the quantitative conclusions of our experiment. For example, the relaxation rates measured in Fig 4b are independent of the way this error is handled.

Due to the cross-Kerr between our readout mode and cavity A we see a slight photon-number dependent reduction in readout contrast. Usually this error happens on measurements where we are selectively measuring the transmon frequency to probe cavity A photon number. By removing the selective transmon rotation and performing readout we can measure the shift in readout contrast due to the cavity occupation.

This cross-Kerr readout error also shows up in Wigner parity measurements. For these we perform two measurements, one mapping $|\text{even}\rangle_A \rightarrow |g\rangle_q$ and $|\text{odd}\rangle_A \rightarrow |e\rangle_q$ while the other performs the map $|\text{even}\rangle_A \rightarrow |e\rangle_q$ and $|\text{odd}\rangle_A \rightarrow |g\rangle_q$. With both of these measurements we can calculate the impact of cavity occupation on readout contrast.

In Fig. 2f we are measuring at times with significant transmon excitation probabilities. This means that the measurement contrast will be effected. We apply the same background measurement that calculates cross-Kerr readout shifts to measure transmon excitation probability. With this we can accurately show the photon addition probability over time. This transmon excitation data is also useful to accurately calculate λ and Ω as shown in Fig. S1.

Because our OCT state preparation have small imperfections, this infidelity in state preparation needs to be taken into account to accurately characterize the PReSPA process. All initial input states in PReSPA characterization experiments are assumed to be non-ideal and measured by transmon spectroscopy (for Fig. 2f and Fig. S1) and Wigner tomography (for Extended Data Fig. 7). Data presented in these figures are re-normalized or transformed by a correction matrix to account for the effect of imperfect state preparation. These state preparation errors are not compensated for in any figure discussing AQEC such as Fig. 4d.

[1]Leghtas, Z. et al. Hardware-Efficient Autonomous Quantum Memory Protection. *Physical Review Letters* **111**, 120501 (2013).
[2]Mirrahimi, M. et al. Dynamically protected cat-qubits: a new paradigm for universal quantum computation. *New Journal of Physics* **16**, 045014 (2014).
[3]Michael, M. H. et al. New Class of Quantum Error-Correcting Codes for a Bosonic Mode. *Physical Review X* **6**, 031006 (2016).
[4]Werschnik, J. & Gross, E. K. U. Quantum optimal control theory. *Journal of Physics B: Atomic, Molecular and Optical Physics* **40**, R175–R211 (2007).
[5]Glaser, S. J. et al. Training Schrödinger's cat: quantum optimal control. *The European Physical Journal D* **69**, 279 (2015).
[6]Gollub, C., Kowalewski, M. & de Vivie-Riedle, R. Monotonic Convergent Optimal Control Theory with Strict Limitations on the Spectrum of Optimized Laser Fields. *Physical Review Letters* **101**, 073002 (2008).
[7]Heeres, R. W. et al. Implementing a universal gate set on a logical qubit encoded in an oscillator. *Nature Communications* **8**, 1–7 (2017).
[8]Leung, N., Abdelhafez, M., Koch, J. & Schuster, D. Speedup for quantum optimal control from automatic differentiation based on graphics processing units. *Physical Review A* **95**, 042318 (2017).
[9]Khaneja, N., Reiss, T., Kehlet, C., Schulte-Herbrüggen, T. & Glaser, S. J. Optimal control of coupled spin dynamics: design of NMR pulse sequences by gradient ascent algorithms. *Journal of Magnetic Resonance* **172**, 296–305 (2005).
[10]Kingma, D. P. & Ba, J. Adam: A Method for Stochastic Optimization. *arXiv:1412.6980 [cs]* (2017).
[11]Baydin, A. G., Pearlmutter, B. A., Radul, A. A. & Siskind, J. M. Automatic differentiation in machine learning: a survey. *The Journal of Machine Learning Research* **18**, 1–43 (2017).
[12]Gao, Y. Y. et al. Programmable Interference between Two Microwave Quantum Memories. *Physical Review X* **8**, 021073 (2018).
[13]Rosenblum, S. et al. A CNOT gate between multiphoton qubits encoded in two cavities. *Nature Communications* **9**, 652 (2018).
[14]Touzard, S. et al. Coherent Oscillations inside a Quantum Manifold Stabilized by Dissipation. *Physical Review X* **8**, 021005 (2018).
[15]Lescanne, R. et al. Escape of a Driven Quantum Josephson Circuit into Unconfined States. *Physical Review Applied* **11**, 014030 (2019).
[16]Wang, C. & Gertler, J. M. Autonomous quantum state transfer by dissipation engineering. *Physical Review Research* **1**, 033198 (2019).
[17]Ofek, N. et al. Extending the lifetime of a quantum bit with error correction in superconducting circuits. *Nature* **536**, 441–445 (2016).
[18]Hu, L. et al. Quantum error correction and universal gate set operation on a binomial bosonic logical qubit. *Nature Physics* **15**, 503–508 (2019).
[19]Macklin, C. et al. A near–quantum-limited Josephson traveling-wave parametric amplifier. *Science* **350**, 307–310 (2015).

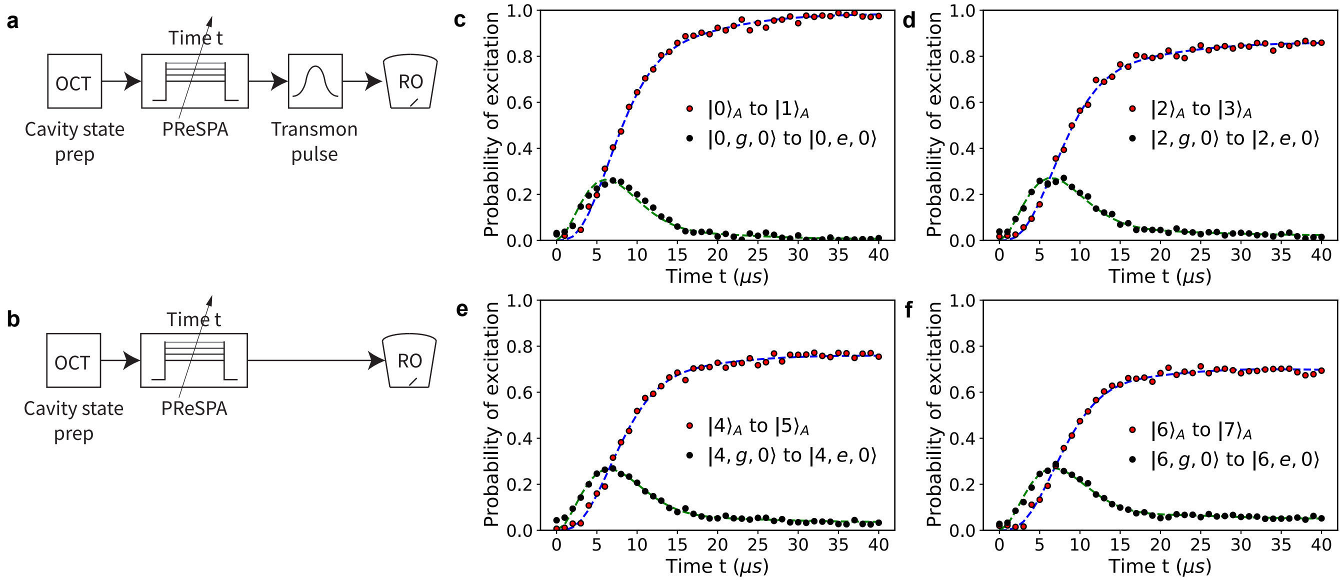

FIG. S1. **Calibration of PReSPA transition rates.** **a**, **b**, Control pulse sequence diagram for tracking the convergence of cavity state towards a target Fock state and the transmon excitation probability over time. For tracking the cavity state (**a**), we prepare initial even Fock states $|0\rangle$, $|2\rangle$, $|4\rangle$, and $|6\rangle$, perform a variable time of PReSPA, and a photon-number selective transmon π-pulse at fixed detunings ($-1\chi_q$, $-3\chi_q$, $-5\chi_q$, and $-7\chi_q$ respectively), and read out the transmon state. For tracking transmon excitations (**b**), the π-pulse is omitted. **c-f**, Transmon excitation probability (black dots) and cavity photon addition probability (red dots) calculated from these two measurement sequences. These measurements are performed for photon conversion from each even state to the next corresponding odd state. The dynamics of excitation transfer is not in the Zeno limit of $\kappa \gg \Omega, \lambda$, but rather can be understood as a slightly-overdamped coupled-oscillator system. To include various detunings and decoherence rates, we fit these curves with a numerically-solved two-stage pumping model (blue and green dashed curves) and extract the PReSPA transition rates (Ω_n and λ_n). The fit contains only three free parameters: Ω_n, λ_n and a y-axis scaling factor. The fit model considers the quantum dynamics across the four relevant levels ($|2n, g, 0\rangle$, $|2n, e, 0\rangle$, $|2n+1, g, 1\rangle$ and $|2n+1, g, 0\rangle$) in a two-stage pumping process. It is simulated with QuTiP and includes the small detuning of the drives due to χ_q', the decay of Cavity A and Reservoir R, and the relaxation, dephasing, and the spurious two-frequency switching behavior (see notes in Extended Data Table I) of the transmon.

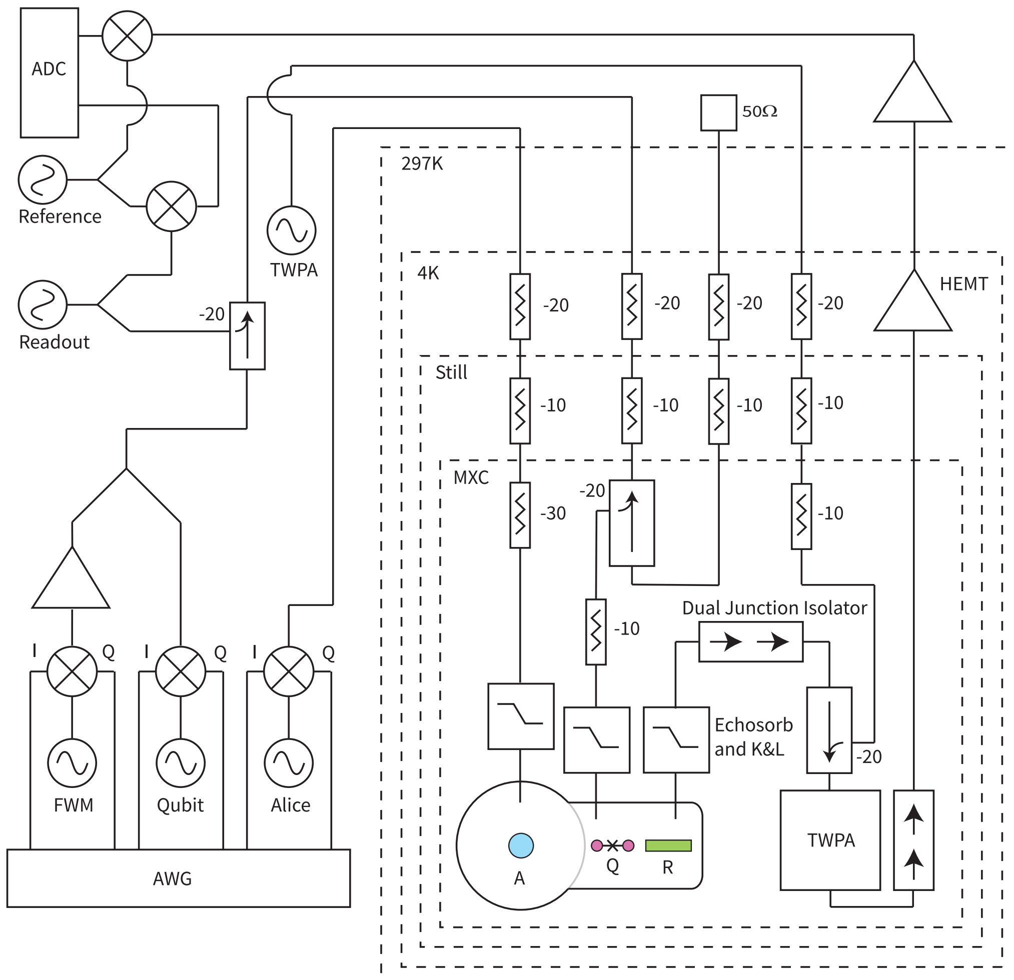

FIG. S2. **Fridge Diagram.** Our experiments are performed in an Oxford Triton-500 dilution refrigerator. Our device is mounted at the mixing chamber (MXC) stage of the refrigerator with a nominal temperature of about 10 mK. We perform a heterodyne transmission measurement of the readout cavity to determine the transmon state. Coherent control signals for both cavity A and the transmon are generated by IQ modulation. Each of the two frequency combs implementing PReSPA is generated by software addition of four frequencies playing on one set of IQ channels (the mixing comb has its own dedicated IQ channels while the transmon comb shares the same IQ channels as the regular transmon qubit gates). We use a first-stage Traveling Wave Parametric Amplifier (TWPA) at base temperature, as well as a High-Electron-Mobility Transistor (HEMT) amplifier at the 4K stage. Our experiment is housed inside a Amuneal A4K shield to protect it from external magnetic fields. All lines connected to the experiment are filtered with a K&L 10 GHz low-pass filter and an Eccosorb low-pass filter.